

Article

Enhanced Photoredox Activity of BiVO₄/Prussian Blue Nanocomposites for Efficient Pollutant Removal from Aqueous Media under Low-Cost LEDs Illumination

Abrar Ali Khan ¹, Leonardo Marchiori ², Elias Paiva Ferreira-Neto ³, Heberton Wender ⁴, Rashida Parveen ⁵, Mohammad Muneeb ¹, Bianca Oliveira Mattos ⁶, Ubirajara Pereira Rodrigues-Filho ⁶, Sidney José Lima Ribeiro ² and Sajjad Ullah ^{1,*}

¹ Institute of Chemical Sciences, University of Peshawar, Peshawar P.O. Box 25120, Pakistan

² Institute of Chemistry, São Paulo State University (UNESP), Araraquara 14800-060, SP, Brazil

³ Department of Chemistry, Federal University of Santa Catarina (UFSC), Florianópolis 88040-900, SC, Brazil

⁴ Nano&Photon Research Group, Laboratory of Nanomaterials and Applied Nanotechnology, Institute of Physics, Federal University of Mato Grosso do Sul, Campo Grande 79070-900, MS, Brazil

⁵ Government Girls Degree College Dabgari, Peshawar 25000, KP, Pakistan

⁶ Institute of Chemistry of São Carlos, University of São Paulo, São Carlos 13560-970, SP, Brazil

* Correspondence: sajjadullah@uop.edu.pk



Citation: Khan, A.A.; Marchiori, L.; Ferreira-Neto, E.P.; Wender, H.; Parveen, R.; Muneeb, M.; Mattos, B.O.; Rodrigues-Filho, U.P.; Ribeiro, S.J.L.; Ullah, S. Enhanced Photoredox Activity of BiVO₄/Prussian Blue Nanocomposites for Efficient Pollutant Removal from Aqueous Media under Low-Cost LEDs Illumination. *Catalysts* **2022**, *12*, 1612. <https://doi.org/10.3390/catal12121612>

Academic Editors: Gassan Hodaifa, Rafael Borja and Mha Albqmi

Received: 19 October 2022

Accepted: 4 December 2022

Published: 8 December 2022

Publisher's Note: MDPI stays neutral with regard to jurisdictional claims in published maps and institutional affiliations.



Copyright: © 2022 by the authors. Licensee MDPI, Basel, Switzerland. This article is an open access article distributed under the terms and conditions of the Creative Commons Attribution (CC BY) license (<https://creativecommons.org/licenses/by/4.0/>).

Abstract: Bismuth vanadate (BiVO₄, BV) is a widely explored photocatalyst for photo(electro)chemical applications, but its full photocatalytic potential is hindered by the fast recombination and low mobility of photogenerated charge carriers. Herein, we propose the photodeposition of different amounts of Prussian blue (PB) cocatalysts on the surface of monoclinic BV to obtain BV-PB composite photocatalysts with increased photoactivity. The as-prepared BV and BV-PB composites were characterized by an array of analytic techniques such scanning electron microscopy (SEM), transmission electron microscopy (TEM), X-ray diffraction (XRD), and spectroscopic techniques including Fourier-transform infrared spectroscopy (FTIR), diffuse reflectance spectroscopy (DRS), electrochemical impedance spectroscopy (EIS), photoluminescence (PL), and Raman spectroscopy. The addition of PB not only increases the absorption of visible light, as indicated by DRS, but also improves the charge carriers' transfer across the photocatalysts/solution interface and hence reduces electron-hole (e⁻-h⁺) recombination, as confirmed by EIS and PL measurements. Resultantly, the BV-PB composite photocatalysts with optimum PB loading exhibited enhanced Cr(VI) photoreduction efficiency as compared to pristine BV under visible light illumination from low-power blue light-emitting diodes (LEDs), thanks to the cocatalyst role of PB which mediates the transfer of photoexcited conduction band (CB) electrons from BV to Cr(VI) species in solution. Moreover, as compared to pristine BV and BV + H₂O₂, a drastic increase in the methylene blue (MB) photo-oxidation efficiency was observed for BV-PB in the presence of a minute quantity of H₂O₂ due to a synergic effect between the photocatalytic and Fenton-like processes. While pure BV photodegraded around 70% of MB dye within 120 min, the BV-PB/H₂O₂ and BV/H₂O₂ system could degrade almost 100% of the dye within 20 min ($k_{\text{obs.}} = 0.375 \text{ min}^{-1}$) and 40 min ($k_{\text{obs.}} = 0.055 \text{ min}^{-1}$), respectively. The practical approach employed in this work may pioneer new prospects for synthesizing new BV-based photocatalytic systems with low production costs and high photoredox efficiencies.

Keywords: photocatalysis; photo-fenton; BiVO₄; Prussian blue; cocatalyst; water purification

1. Introduction

With increasing industrialization and anthropogenic activities across the globe, freshwater bodies have been adversely affected by the uncontrolled contamination with many toxic substances, including both organic (dyes, pharmaceuticals, pesticides, etc.) and inorganic contaminants (heavy metal ions). The presence of these toxic dyes and especially

heavy metal toxins in aqueous environments has become a major global concern that needs to be addressed sooner [1–3]. For example, Cr(VI), which exists in different forms ($\text{Cr}_2\text{O}_7^{2-}$, HCrO_4^- , H_2CrO_4) in aqueous media [4], is highly toxic/carcinogenic, and even poses a threat of genetic modification in aquatic organisms and human beings [5] and is thus considered highly obnoxious and lethal by World Health Organization with a maximum permissible concentration of 0.05 mg/L in aqueous environments [6]. Hence, it is important to find out cost-effective methods to remove hexavalent chromium from water bodies. Consequently, various treatment methods have been introduced for Cr(VI) removal including adsorption [7,8], flocculation [9], chemical precipitation, reverse-osmosis [10,11], electro-coagulation [12], biological treatment [13], membrane separation [11,14], electro-chemical treatment [15,16], ion exchange [17] and photocatalytic reduction processes [18,19]. Similarly, the organic molecules present in aqueous media can be effectively oxidized using advanced oxidation processes (AOPs) which generate highly reactive oxidant species (such as superoxide $\text{O}_2^{\bullet-}$ and super hydroxyl $\bullet\text{OH}$ radicals) for (photo)oxidation of organics [20].

Since Cr(III) is considered to be less toxic and since it can be easily removed as chromium hydroxide via precipitation using conventional techniques of water treatment, photocatalytic reduction of Cr(VI) to Cr(III) is considered a viable strategy to combat Cr(VI) pollution [1,18,19]. This process relies on the transfer of photogenerated electrons from the conduction band of photocatalysts to the Cr(VI) species solution, thereby reducing them to the less toxic Cr(III) form [18]. Unfortunately, the most studied wide-bandgap ($E_g > 3$ eV) semiconductor photocatalysts (such as ZnO and TiO_2) require UV light (which is less than 4% of the solar spectrum) for their photoexcitation and consequent photo(electro)chemical applications, and this practical limitation has attracted researcher's interest to develop visible light active photocatalysts able to use the 45% visible light, so visible light driven photocatalysts are essential to be studied for photocatalytic applications [21–25].

Among the visible light photocatalysts, bismuth vanadate (BV) has gained greater attention due to its narrow band gap (2.4–2.6 eV) and photo(chemical) stability [26]. BV has been widely studied for environmental pollutant degradation, water oxidation, water splitting, and biosensors, among other applications [27–30]. However, BV suffers from fast electron-hole (e^- - h^+) recombination and high resistance to charge transfer to the target species in the solution. To overcome these limitations and bring efficacy in the photoelectrochemical applications of BV, several strategies have been employed, including the loading of metal nanoparticles or metal complexes on BV, hetero-junctions formation [23,26,31–35], metal-ions doping [36–38], and control of BV morphology [39–42].

Prussian blue (PB) is an ancient dye having chemical formulae of $\text{Fe}_4[\text{Fe}(\text{CN})_6]_3$ with three Fe(II) in hexa-coordination with CN and the $\text{Fe}(\text{CN})_6$ octahedral is then combined with four Fe(III) in three-dimensional extended $\text{Fe}(\text{III})-\text{N}\equiv\text{C}-\text{Fe}(\text{II})-\text{C}\equiv\text{N}-\text{Fe}(\text{III})$ linkages, leading to a unit cell with cubic lattice structure [43]. PB is a mixed-valence complex with different ligand-field-strength as a result of the ligand donor environment, where nitrogen-coordinated high-spin d^5 ($S = 5/2$) ferric sites and carbon-coordinated low-spin d^6 ($S = 0$) ferrous sites favor eminent catalytic and electro-magnetic properties [44]. PB-based nanomaterials have been previously explored for (photo)electrochemical applications in conjunction with semiconductor photocatalysts such as TiO_2 and $g\text{-C}_3\text{N}_4$ [18,44–49]. The often-enhanced photoactivity of such systems highlights the transfer of photo-generated electrons from the CB of semiconductor nanomaterials towards the deposited PB cocatalyst layer, thereby reducing PB to Prussian white (PW). The in-situ produced PW species may catalytically transfer electrons to the target species (metal-ions, organic molecules/pollutants) in the solution causing their photoreduction [18]. Similarly, Prussian blue analogues (PBA) have been found to improve the water oxidation efficiency of semiconductor photocatalysts [50–52].

Nevertheless, PB/semiconductor systems other than UV-active TiO_2 -based systems and with high activity in the visible light range remain understudied for photocatalytic applications such as the photoreduction of Cr(VI) and oxidation of organic molecules. Therefore, we present, for the first time, a facile in-situ photodeposition methodology to obtain PB-decorated BV (BV-PB) photocatalysts employing low-cost blue-emitting LEDs

(output 460 ± 10 nm (see Figure S1), total electric power = 1.26 W, light intensity output at 460 nm = $2.5 \text{ mW}/\text{cm}^2$) as illumination source [25]. LEDs have emerged as low-cost, durable, and safer alternatives to conventional lamps for use in photocatalytic applications [53–55], with inherent advantages such as high efficiency in terms of current-to-light emission at relatively lower operational temperature, longer life, small size, and tailorable shapes and, above all, their operation using direct current power supply [56]. The BV-PB system presented herein extended absorption in the visible region, reduced e^- - h^+ recombination, and improved photoactivity towards the mitigation of both organic (photooxidation of MB dye) and inorganic (photoreduction of Cr(VI)) pollutants. Finally, the mechanisms of charge transfer were discussed in detail.

2. Results and Discussion

2.1. Modification of BV with PB

The BV photocatalyst powders were surface modified with PB employing the photo-deposition methodology reported by Tada and co-workers [57]. This method utilizes $[\text{Fe}(\text{CN})_6]^{3-}$ and Fe(III) salts as the molecular precursors and is based on the photo-reduction of $[\text{Fe}(\text{CN})_6]^{3-}$ to $[\text{Fe}(\text{CN})_6]^{4-}$ by the photo-excited electrons in the conduction band (CB) of photocatalyst (BV). The presence of Fe^{3+} cations facilitates the resulting reduced specie to initiate the selective nucleation/growth of PB ($\text{Fe}_4[\text{Fe}(\text{CN})_6]_3$) over the surface BV particles, as depicted in the mechanism shown in Figure 1.

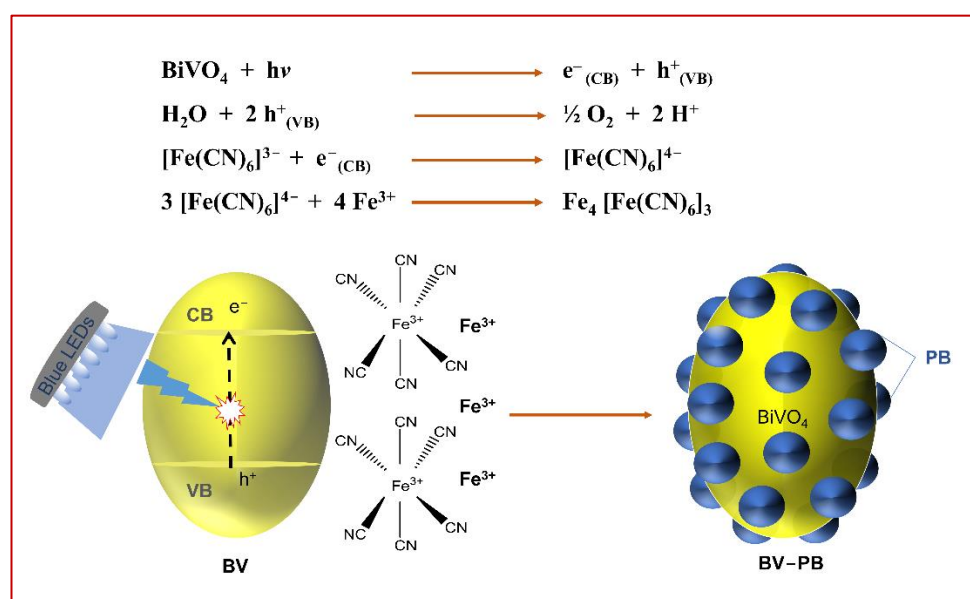


Figure 1. Infographic of the photoexcitation of BV with blue LEDs and the reactions involved in the photo-deposition of PB on the surface of BV.

The formation of PB over the surface of BV was confirmed by FTIR, EDX, XRD, and SEM-EDX analysis, as discussed below.

2.2. Morphological Analysis of BV and BV-PB

The comparison of the representative SEM images of BV and BV-PB3 in Figure 2 clearly shows that the bare BV consists of irregular-shaped hyper-branched BV particles with smooth surfaces (Figure 2a) and their surface roughness drastically increases after modification with PB (Figure 2b), confirming the successful photo-deposition of additional particles (PB) on the surface of BV particles. An analysis of the SEM images of the BV and BV-PB3 samples at different magnifications (Figure S2) confirms that the sample obtained after centrifugation does not contain isolated PB particles. One explanation is that the photo-deposition of PB requires the reduction of Fe^{3+} to Fe^{2+} by the conduction band electrons of

BV, and the photo-deposition most occurs on the surface of BV via heterogeneous nucleation. Furthermore, the SEM images of the different BV-PB samples at the same magnification show a gradual change in morphology, characterized by an increase in the amount of small photo-deposited PB particles as a function of the increasing PB loading (Figure S3).

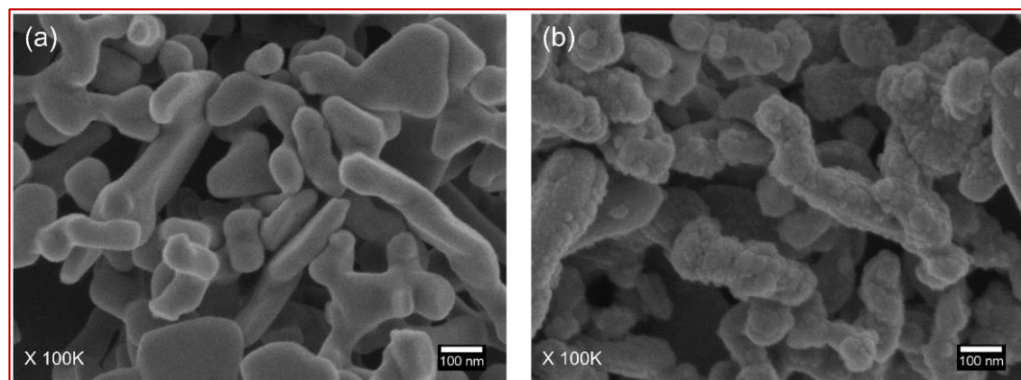


Figure 2. Representative FEG-SEM images of BV (a) and BV-PB3 (b) samples.

TEM analysis was performed to further study the structural features of BV-PB samples. A comparison of the TEM images of BV (Figure 3a) and BV-PB samples (Figure 3b) clearly confirms the formation of smaller than 10 nm PB crystals (average size 8 ± 1 nm) on the surface of BV in the later sample. The high-resolution TEM (HRTEM) image of the BV-PV sample (Figure 3c) shows that these small-surface deposited crystals exhibit interplanar distances of 0.22 nm, ~ 0.3 nm, and 0.38 nm which closely correspond to the (420), (311), and (220) crystal planes of PB, respectively (PDF n. 73-687).

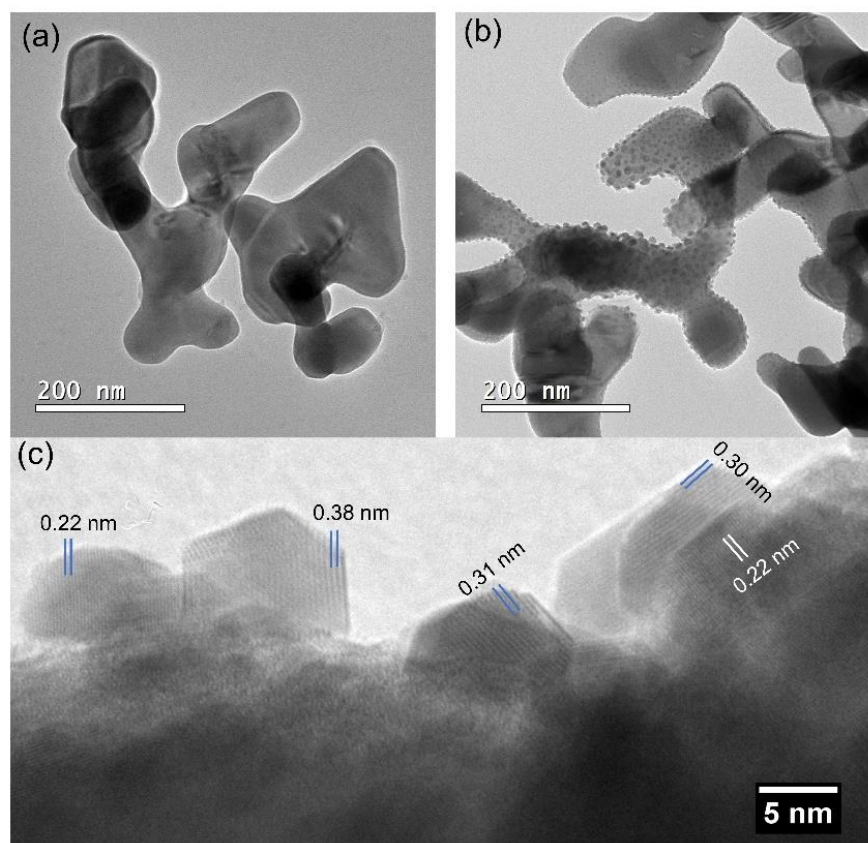


Figure 3. Representative TEM images of BV (a) and BV-PB2 (b) and the HRTEM image of the latter (c).

Qualitative nano-EDX analysis of the selected area of the BV-PB sample shown in the TEM image (Figure S4a) exhibits the X-ray emission lines of Bi, V, O, and Fe (Figure S4b), confirming the elemental identity of BV and the deposition of Fe. The elemental mapping (Figure S4c) performed by monitoring the X-ray lines from Bi ($L\alpha_1$), V ($K\alpha_1$), O ($K\alpha_1$), and Fe ($K\alpha_1$) clearly shows an overlap between the spatial distribution of these elements indicating that the BV-PB sample shown in Figure S4a consists of PB-loaded BV and that Fe (or PB) is present only on the surface of the BV particles.

The bulk elemental composition and PB loading (%Fe content) of the samples were then studied using SEM-EDX microanalysis (Figure 4). The EDX spectrum of pure BV exhibits the X-ray lines of Bi, V, and O with an atomic percentage of 17.7 ± 2.7 , 17.6 ± 2.9 , and 61.7 ± 7.5 %, respectively, giving a chemical composition $\text{BiVO}_{3.6}$ of the prepared BV sample. The EDX spectrum of the BV-PB sample (Figure 4a) shows additional X-ray emission lines at ~ 0.71 and 6.40 keV corresponding to $L\alpha_1$ and $K\alpha_1$ lines of Fe, respectively. The average Fe content (wt.%) and/or the Fe/Bi ratios obtained from triplicate measurements show a quasi-linear trend with the total nominal concentration of Fe precursors ($\text{K}_3[\text{Fe}(\text{CN})_6] + \text{Fe}(\text{NO}_3)_3$ or $(x + y)$ mmol) added during the reaction (Figure 4b), indicating efficient and controlled loading of PB over BV.

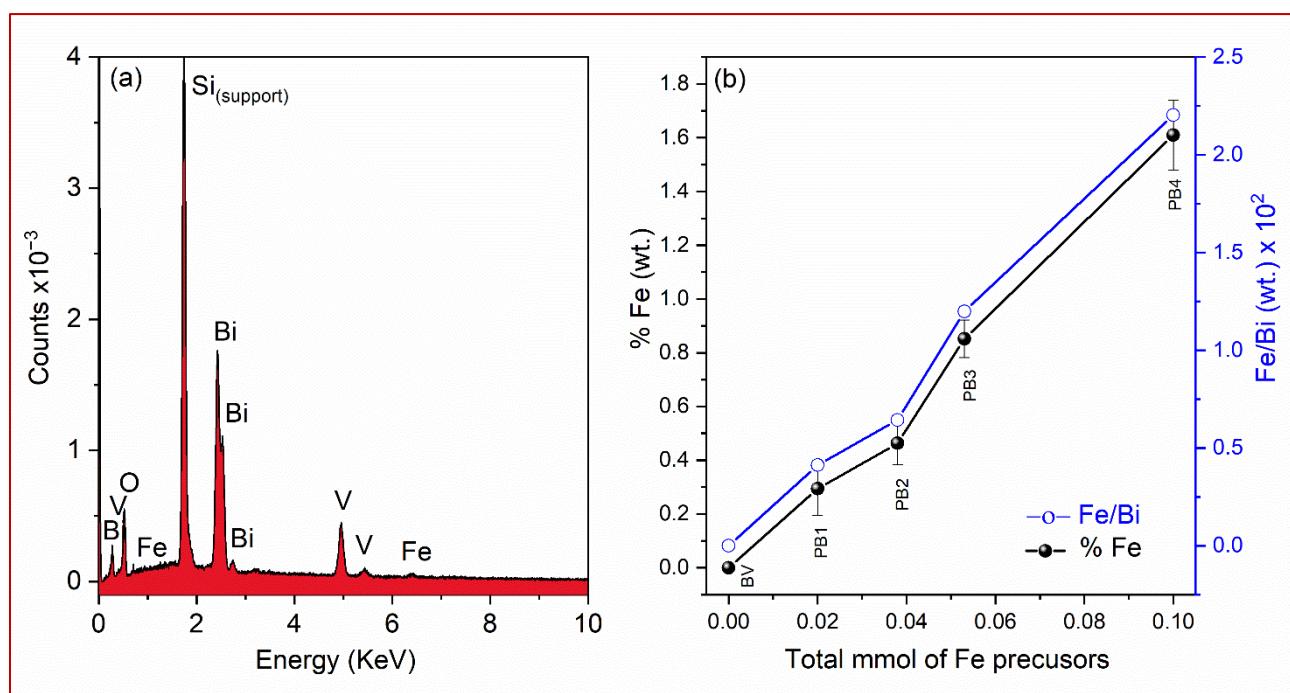


Figure 4. Representative EDX spectrum of BV-PB sample deposited as a thin layer on a silicon wafer (a) and the experimental Fe content (%Fe and Fe/Bi ratio) of different BV-PB samples measured by EDX analysis as a function of the total Fe precursor mmols ($x + y$) of $\text{K}_3[\text{Fe}(\text{CN})_6]$ and $\text{Fe}(\text{NO}_3)_3$, added to in the reaction mixture during the photo-deposition process (b). The Si signal in the (a) comes from the Si wafer used as support.

2.3. Structural and Phase Analysis by XRD

The as-prepared BV and BV-PB samples were analyzed by XRD to further investigate their phase, crystallinity, and crystalline structure (Figure 5). The XRD pattern of the pristine BV sample matches perfectly with the standard diffraction patterns of monoclinic-scheelite BV (PDF no. 75-2480 and 14-0688). The XRD pattern of BV-PB is similar to that of the BV sample but a careful analysis shows the presence of small diffraction features around $2\theta = 17.5^\circ$ (Figures 5 and S5), indicated by (*) and shown magnified in the inset of Figure 5, which corresponds to the most intense diffraction peak originated from the (200) planes of the cubic structure of PB (PDF n. 73-687) [18,58,59], confirming the formation of

PB, in agreement with HRTEM analysis (Figure 3c). The other weak diffraction features of PB expected around 35.4° (400) and 39.8° (420) could not be observed due to an overlap with the diffraction peak of BV (Figure S5) and/or the low PB content ($\text{Fe} < 2\%$) (Figure 4b) [18], lower than the detection limit of XRD ($2 > \%$) for mixed materials.

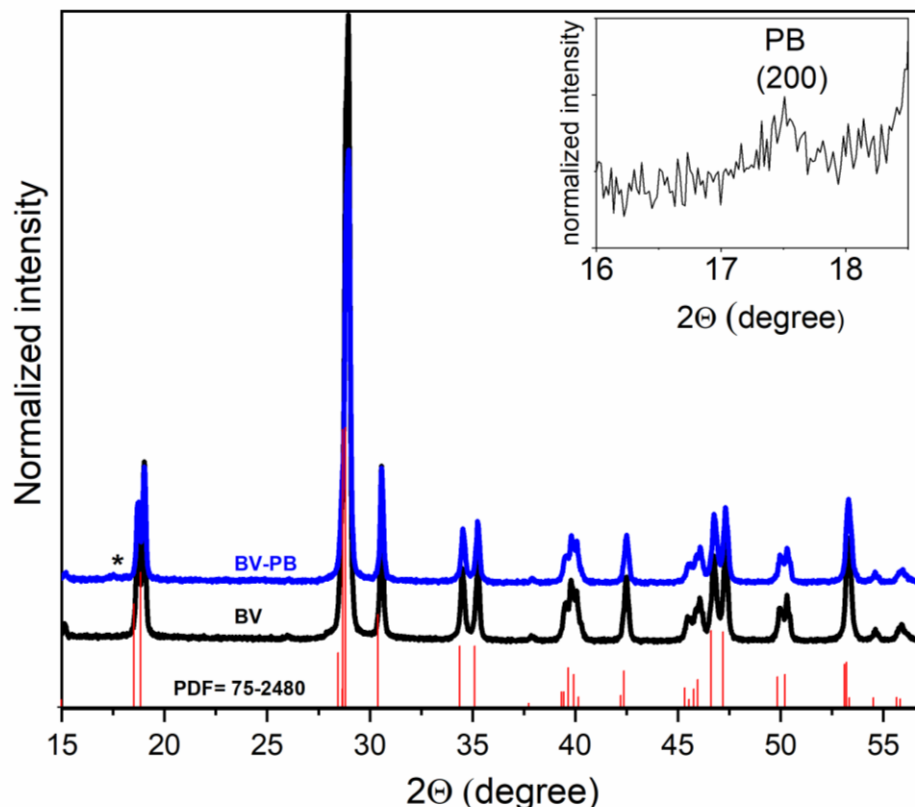


Figure 5. XRD patterns of BV (middle) and BV-PB3 (top) along with standard diffraction pattern of monoclinic BV (PDF 75–2480) (bottom). The inset shows a magnified view of the characteristic most intense diffraction feature of PB (indicated by an * in the diffractogram of BV-PB) at around $2\theta = 17.5^\circ$ corresponding to (200) planes of the cubic structure of PB.

2.4. Vibrational Spectroscopic (Raman and FTIR) Analysis

The formation of PB in BV-PB samples was further studied and confirmed by Raman spectroscopy (Figure 6a) and FTIR spectroscopy (Figure 6b) analysis. Raman spectroscopy is an appropriate methodology for the analysis of the local structure of materials. As shown in Figure 6a, the Raman analysis of unmodified BV shows Raman vibrational bands at 124 cm^{-1} , 209 cm^{-1} , 324 cm^{-1} , 367 cm^{-1} , 706 cm^{-1} , and 825 cm^{-1} (most predominant Raman band), all characteristic of the monoclinic phase of BV [23,60]. The vibrational modes at around 124 cm^{-1} and 209 cm^{-1} are related to the external modes, namely, translational (Ex_t), and rotational (Ex_r) twisting modes, respectively. Indeed, the band at 324 cm^{-1} and 367 cm^{-1} are produced from the asymmetric (δ_{as}) and symmetric (δ_s) bending vibration modes of the V–O bond in the VO_4^{3-} tetrahedra, sequentially. The low-intensity Raman shoulder at 706 cm^{-1} and high-intensity band at 825 cm^{-1} are respectively associated with asymmetric (ν_{as}) and symmetric (ν_s) stretching vibration modes of the V–O bonds, which are particularly sensitive to local-structural variations [50]. The Raman bands of BV-PB samples show the same vibration modes of BV but with a slight shift in band positions (to lower wavenumbers, cm^{-1}) and a decrease in band intensities and widths after PB deposition. For instance, the original stretching vibration modes of the V–O bonds 825 cm^{-1} (BV) shift to 810 cm^{-1} in BV-BP samples. Similarly, the low-intensity Raman shoulder at 706 cm^{-1} disappears and bands at 327 cm^{-1} and 367 cm^{-1} merge in BV-PB sam-

ples. Such spectral changes indicate significant interaction of BV with the photodeposited PB on its surface.

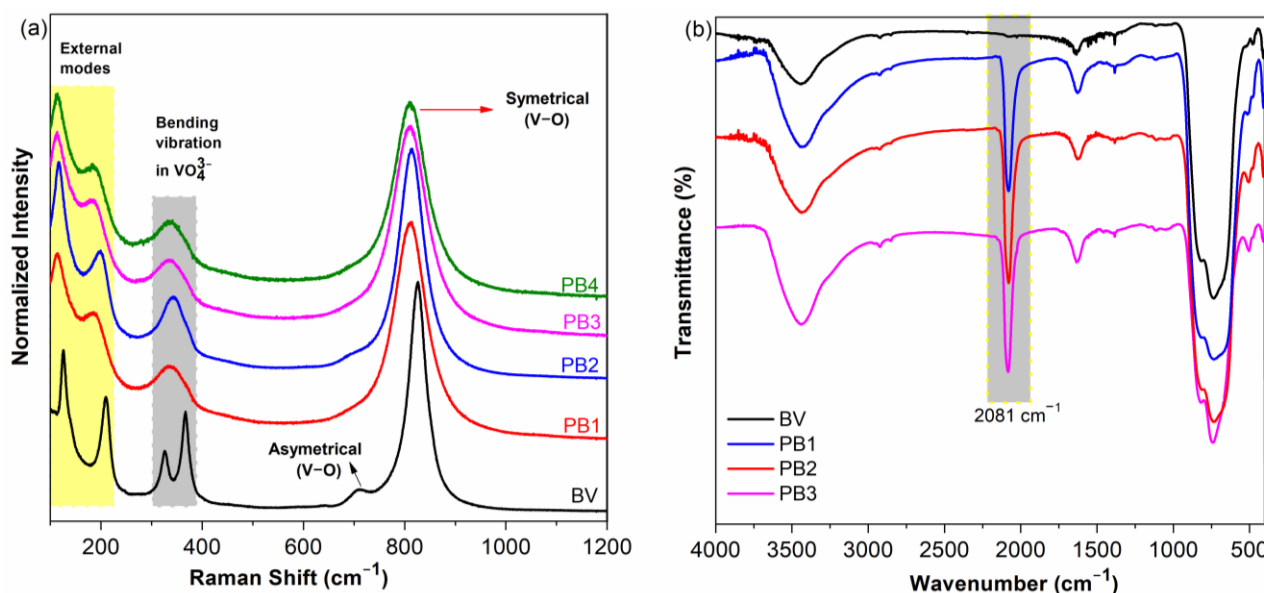


Figure 6. Raman spectra (a) and FTIR spectra (b) of BV and BV-PB samples. The shaded areas in Raman spectra correspond to external modes (yellow) and bending vibrations (gray), respectively. The shaded area in FTIR spectra corresponds to the signature $C\equiv N$ stretching vibrations (2081 cm^{-1}) of PB.

The functional group's analysis of BV and BV-PB samples was performed using FTIR data (Figure 6b). The most important main bands in the $545\text{--}910\text{ cm}^{-1}$ region of the spectra arise from the symmetric stretching (ν_1) and antisymmetric (ν_3) vibration modes of metal-oxygen bond in BV (Figures 6b and S6). More clearly, the pure BV sample exhibits a characteristic strong vibrational band at 736 cm^{-1} , with a shoulder at around 822 cm^{-1} , ascribed to the asymmetric stretching vibration of metal oxide (V–O) groups in BV (see Figure S6) [61]. The bands at 3445 cm^{-1} and 1643 cm^{-1} are ascribed to the symmetric stretching and bending vibrations, respectively, of H–O–H molecules (atmospheric moisture) adsorbed on the surface of the photocatalyst. The small band at 413 cm^{-1} is ascribed to the presence of direct Bi–O linkages [62]. Importantly, the FTIR spectra of all BV-PB samples in Figure 6b exhibit a prominent FTIR band at 2081 cm^{-1} , characteristic of the stretching vibration of $C\equiv N$ bonds (vibrational mode) in the cyanometallate network of PB [18]. The cyanide's vibrational modes at high wavenumbers ($2089\text{--}2070\text{ cm}^{-1}$) are in good agreement with the reported values for pure PB (2070 cm^{-1}) [63], thus confirming the formation of an extended network of PB synthesized via Fe(II)–CN–Fe(III) bridging linkages [18].

2.5. Optical Properties

The effect of PB deposition over BV and the optical characteristics of BV and BV-PB samples were studied using diffuse reflectance UV-visible spectroscopy (DRS) measurements (Figure 7). As shown in the digital images inserted in Figure 7a, the bright yellow BV sample visually turns greenish upon deposition of PB and BV starts to absorb light in the visible region at about $500\text{--}600\text{ nm}$. Maximum absorbance is seen at wavelengths around 470 nm , a value that is comparable with the reported optical band-gap energy ($E_g = 2.5\text{--}2.6\text{ eV}$) of monoclinic BV [23,25,64]. Based on DRS data, the band gap energy (E_g) of BV was calculated by extrapolating the linear portion of the plot between $[F(R)h\nu]^2$ against $h\nu$ to 0 and was found to be 2.6 eV (Figure 7b), in agreement with literature data for monoclinic BV [23,64].

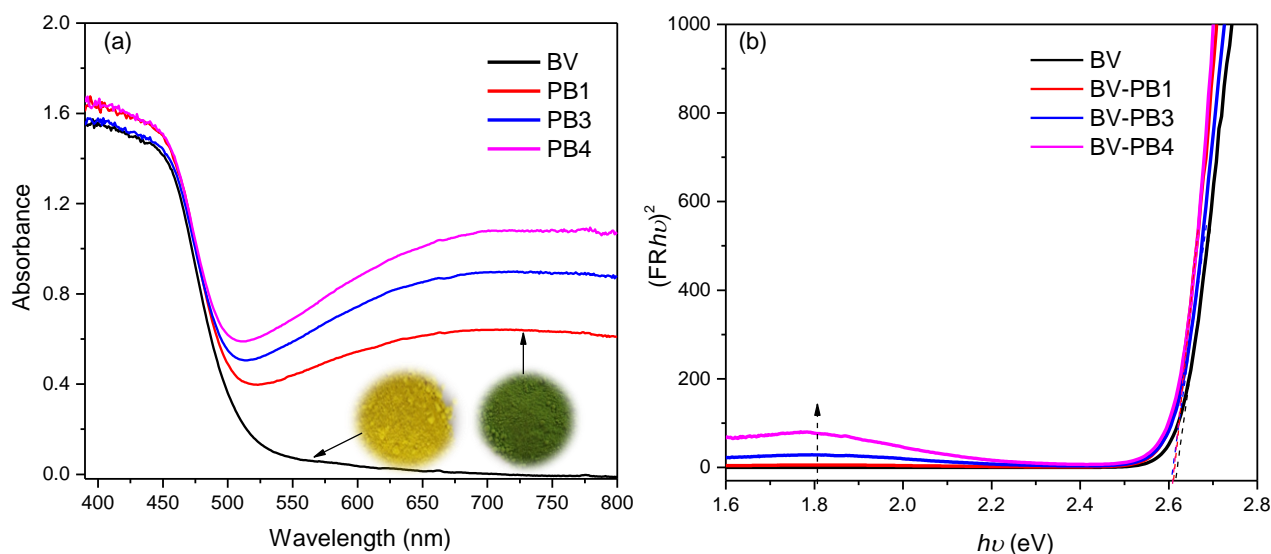


Figure 7. Absorbance spectra of BV and BV-PB samples (a) and the corresponding Kubelka-Munk plot for estimation of the band gap energy (E_g) of BV and BV-PB samples (b). The digital images of BV and BV-PB have been inserted in Figure 7a for visual comparison.

After the deposition of PB onto the BV surface, the visible light absorption of BV-PB samples strongly increases in comparison with BV, which is assigned to the metal-to-metal (Fe^{2+} to Fe^{3+}) intervalence charge transfer in PB. As discussed later, the improved visible-light absorbance of BV-PB is expected to enhance the photoactivity of the composite. Though PB loading increases visible light absorption by the nanocomposite, the absorption edge of BV and BV-PB samples were approximately the same (Figure 7b), with no considerable change in E_g (~ 2.6 eV), indicating only surface deposition of PB without structural modifications of BV.

2.6. Photocatalytic Properties

The photocatalytic properties of BV and BV-PB materials and the role of PB as cocatalyst were evaluated through the photodegradation of MB (Figure 8) and photoreduction of Cr(VI) (Figure 9) in aqueous media under blue LEDs irradiation. The difference in photoactivity of the samples, in terms of interfacial charge transfer at the photocatalysts/solution interface and electron-hole recombination, was then studied and verified using EIS and PL measurements (Figure 10), respectively, in addition to the DRS data presented above. Finally, a comprehensive photoactivity enhancement mechanism was proposed (Figure 11), as discussed at the end of this section.

2.6.1. Photooxidation of MB dye

We first studied the photodegradation of MB using BV and BV-PB samples as photocatalysts in the absence and presence of a minute quantity (0.2 mmol) of H_2O_2 in the reaction mixture under visible light illumination (Figure 8). The absorbance of MB dye decreases upon illumination with blue light from LEDs in the presence of photocatalysts (Figure S7), indicating photodegradation of the dye. While the pure BV could degrade around 70% of MB dye within 120 min (Figure 8b). However, the time for complete photodegradation of MB is reduced to 40 min in the presence of 0.2 mmol H_2O_2 in the reaction mixture (BV+ H_2O_2 , $k_{\text{obs.}} = 0.055 \text{ min}^{-1}$). Compared to pristine BV, the photocatalytic activity increases upon deposition of PB, and BV-PB could degrade around 85% of MB dye within 120 min. Importantly, a very prominent increase in photoactivity of BV-PB is observed in the presence of H_2O_2 and almost 100% degradation of MB is achieved within 20 min ($k_{\text{obs.}} = 0.375 \text{ min}^{-1}$) by the BV-PB/ H_2O_2 system under conditions identical to those of BV + H_2O_2 . Recyclability tests showed that the BV-PB/ H_2O_2 system retains its

photoactivity after repeated use and negligible loss in photoactivity was observed after five cycles of use (Figure 8b).

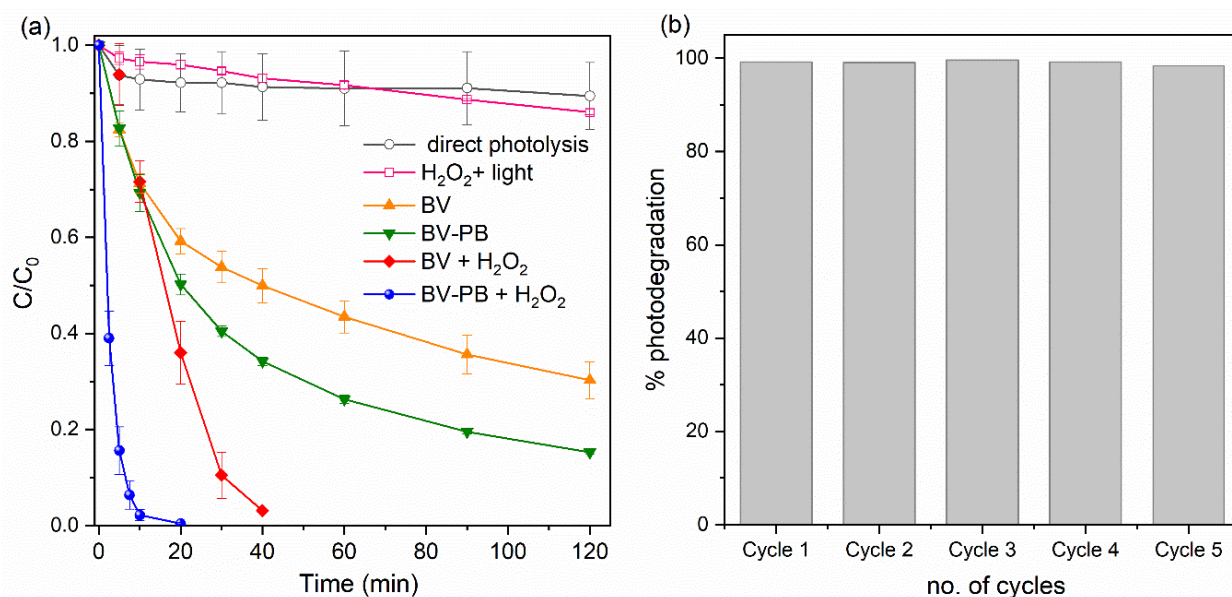


Figure 8. Kinetic profiles showing the photodegradation of MB as a function of visible light illumination time by the pristine BV or BV-PB samples in the presence and absence of a minute amount (0.2 mmol) H_2O_2 in the reaction mixture (a) and the MB photodegradation efficiency of the recycled BV-PB photocatalyst in the presence of H_2O_2 showing good recyclability for up to five cycles of use (b). Results of control experiments employing only LED illumination (direct photolysis), only H_2O_2 and H_2O_2 + LED illumination (emission centered at 460 ± 10 nm) are also reported in (a).

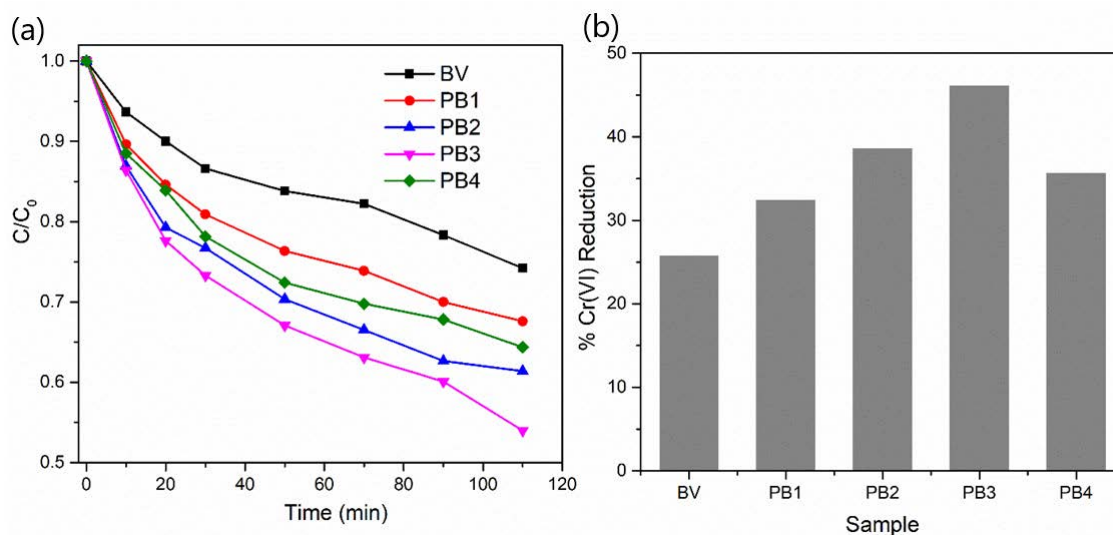


Figure 9. (a) Temporal changes in the concentration of Cr(VI) as a function of LEDs illumination time showing a comparison of the photo-catalytic activities of BV and BV-PB samples (b) A comparison of the Cr(VI) reduction efficiency of BV and different BV-PB samples. The PB layer acts as a cocatalyst, mediating the transfer of photoexcited conduction band electrons from BV to Cr(VI) (see also Figures 10 and 11). The experiments were performed without any pH adjustment (natural pH = 4.6) of the suspension and without adding any hole scavenger organic molecules. The experiments under light irradiation were performed using the LED reactor described above.

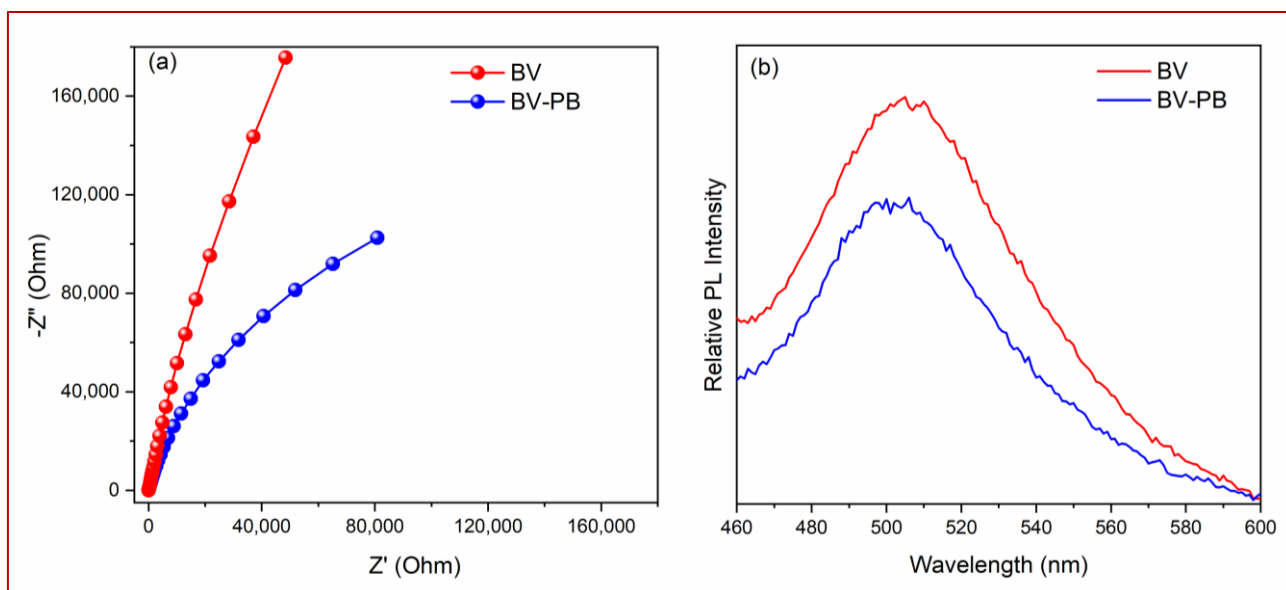


Figure 10. Nyquist plot obtained from EIS measurements under dark condition (a) and PL emission spectra arising from electron-hole recombination (b) of representative BV and BV-PB3 samples.

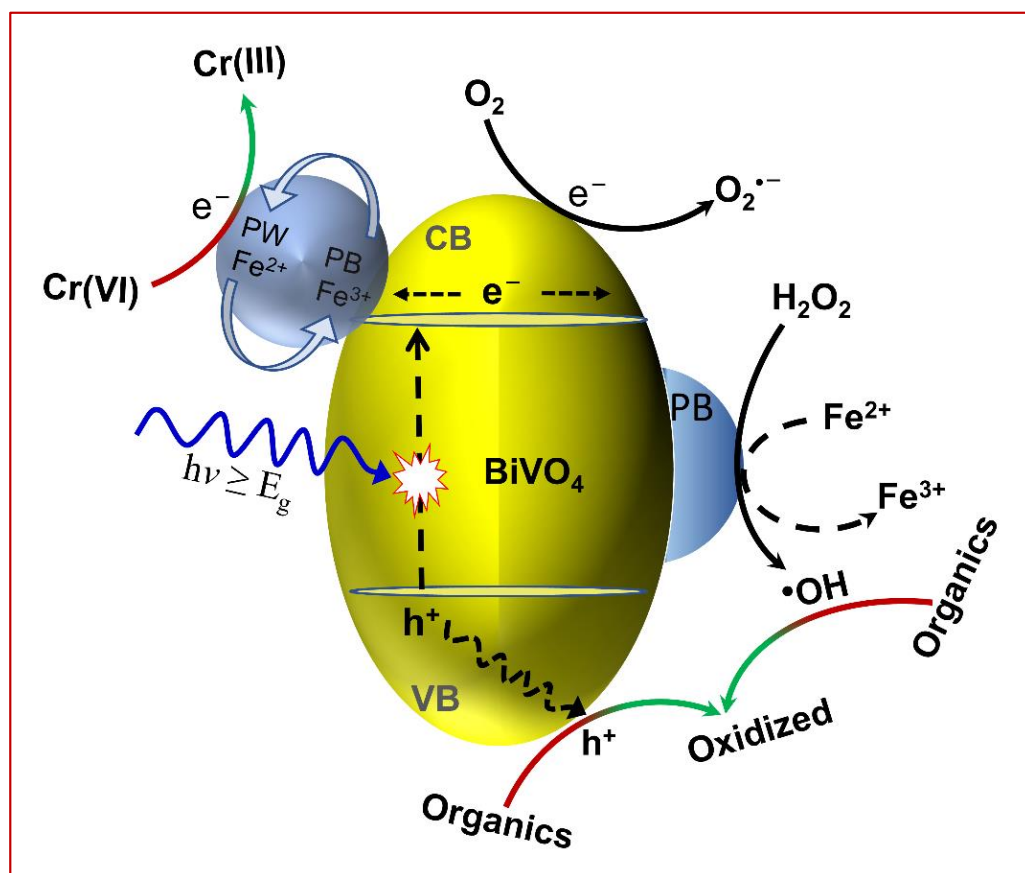


Figure 11. Schematics of the photoexcitation, charge transfer, and resulting photocatalytic processes in the BV/PB system. The photoexcited electrons from CB of BV transfer to PB and dissolved O_2 reducing them to PW and $\text{O}_2^{\bullet-}$, respectively. The PW, in turn, transfers electrons to Cr(VI) in a solution, itself becoming oxidized back to PB. Hydrogen peroxide is converted to $\bullet\text{OH}$ radicals which, together with holes (h^+) in the valence band, can oxidize organic materials.

2.6.2. Photoreduction of Cr(VI)

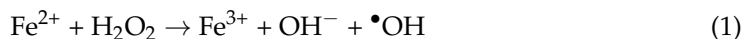
Next, the photoreduction of toxic Cr(VI) to less toxic Cr(III) in aqueous media was studied under LED illumination apparatus and without any pH adjustment or addition of sacrificial organic molecules. Figure S8 shows the decrease in absorbance of the chromium (Cr)-DPC complex as a function of time under visible light illumination in the presence of BV-PB3 as representative photocatalysts, indicating photoreduction of Cr(VI) to Cr(III). All BV-PB samples exhibit better photoactivity than pristine BV (Figure 9) demonstrating that the PB assists in the photoreduction of Cr(VI), as explained below. The photoreduction efficiency of the samples follows the order BV-PB3 > BV-PB2 > BV-PB4 > BV-PB1 > BV.

2.7. Why BV-PB Shows Enhanced Photoactivity?

The above-noted superior photo-redox efficiency of the BV-PB samples, as compared to BV, could arise from:

1. Enhanced absorption of visible light (Figure 7),
2. The ability of Fe centers in PB to produce reactive oxygen species (ROS) in a Fenton-like derived process,
3. The role of PB as cocatalysts, lowering resistance to charge transfer and improving charge transfer ability at the photocatalysts/solution interface, thus promoting electron transfer from the conduction band (CB) of BV to the Cr(VI) and/or O₂ species in solution, and/or
4. Decreased electron-hole recombination due to lower charge transfer resistance.

While the enhanced visible light absorption (factor 1) is evident from Figure 7, an equally important PB-based Fenton-like process (factor 2) could occur at the Fe centers in PB in the presence of H₂O₂. This process generates additional ROS (\bullet OH and HOO \bullet) via oxidation of Fe²⁺ to Fe³⁺ (Equation (1)), and/or reduction of Fe³⁺ (Equation (2)).



We have already observed that the photogenerated holes and ROS species (\bullet OH and O₂ \bullet^-) play a role in the photocatalytic degradation of dyes over BiVO₄ photocatalyst [23]. Since additional \bullet OH species are expected to form in BV-PB material, the formation of \bullet OH in the reaction mixture was confirmed by using terephthalic acid (TPA) as a fluorescent probe which reacts with \bullet OH radicals to form 2-hydroxy terephthalic acid of relatively higher fluorescence intensity. The fluorescence intensity of TPA increases a little in the presence of only H₂O₂ but drastically in the presence of both BV-PB and H₂O₂ in the reaction mixture (Figure S9), confirming our hypothesis of the Fenton-like process in the BV-PB/H₂O₂ system. Thus, the excellent photoactivity of the BV-PB/H₂O₂ system can be assigned to a synergic effect between the BV-based photocatalytic (h⁺ and \bullet OH/O₂ \bullet^- generation) and PB-based Fenton-like processes (Figure 11, RHS), in addition to the other factors, such as lower electron-hole recombination and lower charge transfer resistance at photocatalysts/solution interface (*vide infra*). Furthermore, the improved interfacial charge transfer between BV and photo-deposited PB, as discussed below, may further increase the overall photo-Fenton process as it leads to the regeneration of Fe(II) sites (Equation (3)), which are known to be much more catalytic, active for hydroxyl radical formation in the presence of H₂O₂ [65].

The other two hypotheses (or factors 3 and 4) highlighting the role of PB as a cocatalyst were evaluated using EIS measurements (Figure 10a) and PL measurements (Figure 10b), respectively. Factor 3 was evaluated by measuring the charge transferability of BV and BV-PB samples from the Nyquist plot using EIS measurements (Figure 10a). As compared to pure BV, the BV-PB samples show lower resistance to charge transfer and the charge transfer ability seems to improve the photoreduction of the target specie (Cr(VI) and/or O₂) in the

solution [18]. Such improved charge transfer kinetics are expected to allow better charge separation and hence lower recombination (factor 4). The PL measurement of BV and BV-PB showed that the latter has lower PL intensity (that arises from electron-hole recombination) as compared to BV (Figure 10b), indicating reduced electron-hole recombination in BV-PB. The decrease in photoactivity at higher PB loading (BV-PB4 in Figure 9) may be related to the lower accessibility of photogenerated CB electron for Cr(VI) reduction in aqueous media due to a less effective transfer across relatively thicker BV/PB interface.

Considering the discussion above, it can be asserted that the blue LEDs illumination (λ output = 460 ± 10 nm which overlaps the absorption of BV ($E_g = 2.6$ eV)) can photoexcite electrons from the valance band (VB) of BV to its CB (Figure 11). The photoexcited electrons in the CB are subsequently transferred to molecular O_2 forming $O_2^{\bullet-}$ and to PB, partially reducing it ($Fe^{3+} + e^-_{(CB)} \rightarrow Fe^{2+}$) to Prussian white (PW). The resulting PW, in turn, transfers the extra electrons to Cr(VI) (and/or O_2) species in solution, reducing Cr(VI) to Cr(III) (and/or O_2 to $O_2^{\bullet-}$) and itself reverts back to PB for the next redox cycle (Figure 11, LHS). The mechanism proposed for charge transfers is represented in Figure 11. PB thus acts as a cocatalyst, mediating the transfer of electrons from BV to Cr(VI) (Figure 10a) and decreasing the electron-hole recombination (Figure 10b).

The practical approach employed in this work may guide new studies and pioneer new prospects for synthesizing new BV-based photocatalytic systems with low production costs and high photoredox efficiencies.

3. Materials and Methods

3.1. Reagents

Potassium hexacyanoferrate(III) ($K_3[Fe(CN)_6]$, 99%), iron(III) nitrate ($Fe(NO_3)_3 \cdot 9H_2O$), and 1,5-diphenylcarbazine (DPC) were supplied by Sigma-Aldrich (São Paulo, Brazil). Ammonium metavanadate (NH_4VO_3 , 99%, Merck, Darmstadt, Germany), $Bi(NO_3)_3 \cdot 5H_2O$ (>98%, Neon, São Paulo, Brazil), HNO_3 (Qhemis, São Paulo, Brazil), NH_4OH (28%, Synth, São Paulo, Brazil), acetone (Synth), H_2O_2 (50%, Synth), and potassium dichromate ($K_2Cr_2O_7$, Mallinckrodt, France) were used as received.

3.2. Preparation of BV and BV-PB Photocatalysts

Monoclinic BV nanoparticles were synthesized via the precipitation-hydrothermal route reported in our previous work [25]. Briefly, an aqueous solution of NH_4VO_3 (1 mmol) was drop-wise added to an equimolar aqueous solution of $Bi(NO_3)_3 \cdot 5H_2O$ under continuous stirring to give an orange-yellow solution, followed by pH adjustment (pH ~ 6), and then microwave-assisted hydrothermal treatment (180 °C, 125 W, 275 psi, 10 min). The resulting bright yellow BV suspension (was centrifuged (6000 rpm), washed with deionized water twice, and dried at 80 °C for 24 h).

The BV-PB samples were prepared by a photo-assisted deposition method employing an array of home-made LEDs (output = 460 ± 10 nm (Figure S1), total electric power = 1.26 W, light intensity output at 460 nm = 2.5 mW/cm²) as described elsewhere [25], using $K_3[Fe(CN)_6]$ and $(Fe(NO_3)_3 \cdot 9H_2O)$ as the PB precursors. For this purpose, 150 mg of BV powder was dispersed in 100 mL water by sonication for 30 min, followed by the addition of different amounts (x mmol) of potassium $K_3[Fe(CN)_6]$ and stirring the mixture for 1h in dark (suspension A). Then, different amounts of $Fe(NO_3)_3 \cdot 9H_2O$ solution (30 mL solution in 0.03M HNO_3 containing y mmol of the precursor) were drop-wise added to suspension A under LED illumination and, after 1h illumination at 460 nm, the resulting suspension of BV-PB composite was separated via centrifugation, washed twice with deionized water and then dried in an oven at 80 °C. The molar concentrations of $K_3[Fe(CN)_6]$ (x mmol) and $Fe(NO_3)_3 \cdot 9H_2O$ (y mmol) were kept equal (1:1) for each set of samples and varied in a certain range ($x = y = 0.01, 0.019, 0.026, 0.05$ mmol) to prepare different samples (BV-PB1, BV-PB2, BV-PB3, BV-PB4, respectively) with different PB loadings.

3.3. Characterization Techniques

Scanning electron microscopy (SEM) images were obtained using a FEG-SEM microscope (JSM-7200, JEOL, USA). The samples, deposited on silicon wafer pieces, were sputter-coated with 6 nm gold layer using BAL-TEC MED 020 (BAL-TEC, Balzers Liechtenstein) coating System (conditions: chamber pressure = 2.00×10^{-2} mbar; current = 60 mA; deposition rate 0.60 nm/s). Energy Dispersive X-ray Spectroscopy (EDX) microanalysis was performed using an XFlash[®] 6/60 detector (Bruker, Germany), employing ESPRIT 2.3 software, using a 15 kV electron beam, and using Cu standard for analytical calibration. For EDX analysis, the samples were pressed into a thick pellet and attached to the surface of conducting carbon tape. Three different regions ($50 \mu\text{m} \times 50 \mu\text{m}$) of the same sample were analyzed to obtain an average elemental composition [23]. TEM analysis of the sample deposited from a dilute aqueous suspension onto carbon-coated copper grids was performed on a JEOL TEM (JEM-2100, USA) equipped with a LaB₆ electron source and operated at 200 kV electron accelerating voltage. X-ray diffraction (XRD) patterns of BV and BV-PB samples were measured using a D8 Advance X-ray diffractometer (Bruker, Germany) operating at 40 mA and 40 kV and employing Ni-filtered Cu K α X-ray radiation (1.540 Å). The diffuse reflectance spectra (DRS) of the powder samples against a background of MgO powder (white standard) were obtained using a Cary 5000 UV-Vis-NIR spectrophotometer (Varian, Australia). Raman spectra ($100\text{--}1200 \text{ cm}^{-1}$, acquisition time of 40 s, 2 cycles) were measured with a LabRAM HR 800 Raman spectrophotometer (Horiba Jobin Yvon) equipped with a He-Ne laser (632.81 nm). The photoluminescence (PL) emission spectra ($\lambda_{\text{excitation}} = 375 \text{ nm}$) of the samples were acquired with a Horiba Jobin Yvon spectrofluorometer (Fluorolog-3 model FL3-122, USA) equipped with a Hamamatsu R-928 photomultiplier tube and a Xe lamp. Electrochemical impedance spectroscopy (EIS) measurements of the sample films on FTO glass were performed in a CorrTest potentiostat/galvanostat (model CS310, Wuhan China) using a three-electrode cell [23]. Fourier transform infrared spectroscopy (FTIR) spectra ($400\text{--}4000 \text{ cm}^{-1}$) of the samples diluted with KBr and pressed into a pellet were collected with a NICOLET IS5 FTIR spectrophotometer (Thermo Scientific, Waltham, MA, USA) with a resolution of 2 cm^{-1} and averaged over 64 scans.

3.4. Evaluation of Photocatalytic Activity

The photocatalytic activity of BV and BV-PB samples was evaluated by photoreduction of Cr(IV) ions and photooxidation of MB dye as a model photocatalytic reaction.

3.4.1. Photocatalytic Reduction of Cr(VI)

The photoreduction of Cr(VI) was performed in order to evaluate the photoreduction efficiency of the BV and BV-PB and hence the role of PB in the composite photocatalysts. For this purpose, typically, 35 mg of the photocatalysts powder was dispersed in 35 mL of H₂O by sonication followed by the addition of 35 mL K₂Cr₂O₇ containing $20 \text{ mg}\cdot\text{L}^{-1}$ of Cr(VI). The resultant mixture (natural pH 4.6) was kept in the dark for 30 min and then illuminated with blue LEDs described above for different time intervals. The sample aliquots taken at various irradiation intervals were centrifuged to remove the suspended particle and 200 μL of the supernatant was then reacted with DPC ($5 \text{ g}\cdot\text{L}^{-1}$ in acetone) as a selective colorimetric reagent [66] in the presence of H₂SO₄ in the reaction media (1 mL H₂O + 200 μL DPC + 100 μL H₂SO₄) to form Cr(VI)-DPC complex that shows maximum absorbance at 545 nm. During the reaction, Cr(VI) is reduced to Cr(III) and DPC is oxidized to 1,5-diphenylcabazone (DCPA). The decrease in the concentration of Cr(VI) was measured by observing the decrease in the absorbance ($\lambda_{\text{max}} = 545 \text{ nm}$) of the Cr-DPC complex [18].

3.4.2. Photocatalytic Degradation of Methylene Blue (MB)

The photocatalytic activity of BV-PB and pure BV was also evaluated by the photodegradation of MB dye in the absence and presence of a minute amount of H₂O₂ in the reaction mixture. Typically, 25 mg of the photocatalyst was dispersed in 20 mL water by sonicated for 15 min, followed by the addition of 20 mL MB dye ($15 \text{ mg}\cdot\text{L}^{-1}$) and allowing

the dye-photocatalyst mixture to stir in dark for 30 min. The mixture was then irradiated with the blue LEDs photoreactor described above and sample aliquots were taken out, centrifuged, and electronic absorption spectra of the supernatant measured to follow the degradation of MB as a function of time. In the degradation studies performed in the presence of H₂O₂, 200 µL of 1 mol·L⁻¹ H₂O₂ solution was added to the reaction mixture just before illumination. A control experiment in the absence of photocatalysts in the reaction mixture was also performed under identical conditions to better evaluate the role of photocatalysts (BV, BV-PB), H₂O₂, and direct photolysis in the total MB removal efficiency of the photocatalytic systems studied. To compare the photoactivity of the samples towards MB degradation, the observed rate-constant (k_{obs}) values were calculated from the kinetic profiles ($\frac{C}{C_0}$ vs. time) using a first order exponential-function, ($\frac{C}{C_0} = e^{-k_{\text{obs}} \cdot t}$).

The recyclability of the photocatalysts was tested by the same procedure just mentioned above, except that the used photocatalysts were recovered from the reaction mixture by centrifugation at 4500 rpm for 10 min, re-dispersed in 20 mL water by sonication, mixed with 20 mL MB (15 mg·L⁻¹) and then employed in the next photocatalytic degradation cycles in the presence of H₂O₂ under LED illumination for 25 min.

To study the formation of •OH radicals by the BV-PB photocatalysts in the presence of H₂O₂, terephthalic acid (TPA, 4 × 10⁻⁴ mol·L⁻¹ solution in 2 × 10⁻³ mol·L⁻¹ NaOH) was used a fluorescence probe molecule [67]. The fluorescence spectra (340–600 nm, $\lambda_{\text{max(emission)}} = 425$ nm) of TPA were recorded under 315 nm excitation [67] in the absence and presence of BV-PB and H₂O₂.

4. Conclusions

Addressing the inherent problems of BiVO₄ (BV) photocatalysts, including fast electron-hole recombination and slow charge transfer kinetics, we successfully prepared PB-loaded BV particles with enhanced photo-redox ability as investigated by photoreduction of Cr(VI) and photooxidation of MB. The PB was photo-deposited on the surface of hydrothermally synthesized monoclinic BV using low-cost commercial LEDs as the illumination source and the formation of BV-PB was confirmed by microscopic and spectroscopic analyses. The photo-deposited PB not only increases the absorption of visible light by the BV-PB composite photocatalyst, as indicated by DRS but also acts as cocatalysts, improving the charge carriers' transfer across the photocatalysts/solution interface and hence reducing their recombination, as confirmed by EIS and PL measurements, respectively. Consequently, the BV-PB composite photocatalysts with optimum PB loading exhibited enhanced Cr(VI) photoreduction efficiency as compared to pristine BV under visible light illumination from low-power LEDs, thanks to the cocatalyst role of PB which mediates the transfer of photoexcited conduction band electrons from BV to Cr(VI) species in solution. As compared to pristine BV (70% of MB degradation in 120 min), higher photoactivity was observed in the presence of a minute amount (0.2 mmol) of H₂O₂ in the reaction media for both BV (~97% photodegradation in 40 min, $k_{\text{obs}} = 0.055$ min⁻¹) and BV-PB (100% dye degradation within 20 min, $k_{\text{obs}} = 0.375$ min⁻¹) materials. Such high photo-oxidation efficiency of the BV-PB/H₂O₂ system is due to a synergic effect between the BV-based photocatalytic and PB-based Fenton-like processes, in addition to other factors including the role of PB as cocatalysts discussed above. The practical approach reported in this study may be extended to other photocatalytic systems with high photoredox efficiencies for photo(electro)chemical applications.

Supplementary Materials: The following supporting information can be downloaded at: <https://www.mdpi.com/article/10.3390/catal12121612/s1>, Figure S1: The emission spectrum of LEDs; Figures S2 and S3: SEM images of BV and BV-PB; Figure S4: TEM images and elemental mapping of BV-PB, Figure S5: XRD patterns of BV and BV-PB; Figure S6: FTIR Spectrum of pure BV; Figure S7: Electronic absorption spectra of MB dye as a function of LED illumination, Figure S8: Absorption spectra of Cr(VI)-DPC complex; Figure S9: Fluorescence spectra of pure terephthalic acid in the presence and absence of BV-PB2 and H₂O₂.

Author Contributions: Methodology, A.A.K. and L.M.; investigation, A.A.K., M.M., L.M. and B.O.M.; writing, review and editing, A.A.K., E.P.F.-N., H.W., R.P., U.P.R.-F. and S.J.L.R.; conceptualization, S.U. and E.P.F.-N.; funding acquisition and supervision, S.U., S.J.L.R. and U.P.R.-F. The manuscript was written through the contributions of all authors. All authors have read and agreed to the published version of the manuscript.

Funding: This research was funded by Higher Education Commission (HEC), Pakistan (Project No. 9286), the São Paulo Research Foundation (FAPESP, Brazil) (FAPESP Process 15/22828-6). H. Wender acknowledges financial support from CNPq (Projects 486342/2013-1, 427835/2016-0, 311798/2014-4, 313300/2020-8, and 310066/2017-4); FUNDECT (N. 099/2014, 106/2016, and 228/2022), and Coordenação de Aperfeiçoamento de Pessoal de Nível Superior—Brasil (CAPES)—Finance Code 001 and Capes-PrInt program (grant numbers 88881.311921/2018-01 and 88887.311920/2018-00). L. Marchiori also thanks CNPq for the Ph.D fellowship (grant number 140851/2021-6).

Data Availability Statement: The data supporting reported results can be shared on demand.

Acknowledgments: Sajjad Ullah also acknowledges the São Paulo State University (IQ-UNESP), Araraquara, SP, Brazil for the support and opportunity to work as a short-term visiting researcher.

Conflicts of Interest: The authors declare no conflict of interest.

References

1. Saiz, P.G.; Valverde, A.; Gonzalez-Navarrete, B.; Rosales, M.; Quintero, Y.M.; Fidalgo-Marijuan, A.; Orive, J.; Reizabal, A.; Larrea, E.S.; Arriortua, M.I.; et al. Modulation of the Bifunctional CrVI to CrIII Photoreduction and Adsorption Capacity in ZrIV and TiIV Benchmark Metal-Organic Frameworks. *Catalysts* **2021**, *11*, 51. [CrossRef]
2. Ukhurebor, K.E.; Aigbe, U.O.; Onyancha, R.B.; Nwankwo, W.; Osibote, O.A.; Paumo, H.K.; Ama, O.M.; Adetunji, C.O.; Siloko, I.U. Effect of Hexavalent Chromium on the Environment and Removal Techniques: A Review. *J. Environ. Manag.* **2021**, *280*, 111809. [CrossRef] [PubMed]
3. Liu, D.; Wang, Y.; Xu, X.; Xiang, Y.; Yang, Z.; Wang, P. Highly Efficient Photocatalytic Cr(VI) Reduction by Lead Molybdate Wrapped with D-A Conjugated Polymer under Visible Light. *Catalysts* **2021**, *11*, 106. [CrossRef]
4. Szabó, M.; Kalmár, J.; Ditrói, T.; Bellér, G.; Lente, G.; Simic, N.; Fábrián, I. Equilibria and Kinetics of Chromium(VI) Speciation in Aqueous Solution—A Comprehensive Study from PH 2 to 11. *Inorganica Chim. Acta* **2018**, *472*, 295–301. [CrossRef]
5. Mishra, S.; Bharagava, R.N. Toxic and Genotoxic Effects of Hexavalent Chromium in Environment and Its Bioremediation Strategies. *J. Environ. Sci. Health Part C* **2016**, *34*, 1–32. [CrossRef]
6. WHO Expert Consultation for 2nd Addendum to the 3rd Edition of the Guidelines for Drinking-Water Quality: Geneva, 15–19 May 2006, WHO/SDE/WSH/06.05 v, 136 p. Available online: <https://Apps.Who.Int/Iris/Handle/10665/69604> (accessed on 28 July 2022).
7. Ambika, S.; Kumar, M.; Pisharody, L.; Malhotra, M.; Kumar, G.; Sreedharan, V.; Singh, L.; Nidheesh, P.V.; Bhatnagar, A. Modified Biochar as a Green Adsorbent for Removal of Hexavalent Chromium from Various Environmental Matrices: Mechanisms, Methods, and Prospects. *Chem. Eng. J.* **2022**, *439*, 135716. [CrossRef]
8. Omer, A.M.; Abd El-Monaem, E.M.; Eltaweil, A.S. Novel Reusable Amine-Functionalized Cellulose Acetate Beads Impregnated Aminated Graphene Oxide for Adsorptive Removal of Hexavalent Chromium Ions. *Int. J. Biol. Macromol.* **2022**, *208*, 925–934. [CrossRef]
9. Du, J.; Shang, X.; Shi, J.; Guan, Y. Removal of Chromium from Industrial Wastewater by Magnetic Flocculation Treatment: Experimental Studies and PSO-BP Modelling. *J. Water Process Eng.* **2022**, *47*, 102822. [CrossRef]
10. Salman, R.H.; Hassan, H.A.; Abed, K.M.; Al-Alawy, A.F.; Tuama, D.A.; Hussein, K.M.; Jabir, H.A. Removal of Chromium Ions from a Real Wastewater of Leather Industry Using Electrocoagulation and Reverse Osmosis Processes. *AIP Conf. Proc.* **2020**, *2213*, 020186. [CrossRef]
11. Hu, W.; Chen, Y.; Dong, X.; Meng, Q.W.; Ge, Q. Positively Charged Membranes Constructed via Complexation for Chromium Removal through Micellar-Enhanced Forward Osmosis. *Chem. Eng. J.* **2021**, *420*, 129837. [CrossRef]
12. Zhang, C.; Li, Q.; Chen, Q. Electrochemical Treatment Of Landfill Leachate To Remove Chromium (Vi) Using Ni₃n And Nio Nps Anodes. *Int. J. Electrochem. Sci.* **2021**, *16*, 210710. [CrossRef]
13. Zhao, Y.; Gao, J.; Zhou, X.; Li, Z.; Zhao, C.; Jia, X.; Ji, M. Bio-Immobilization and Recovery of Chromium Using a Denitrifying Biofilm System: Identification of Reaction Zone, Binding Forms and End Products. *J. Environ. Sci.* **2023**, *126*, 70–80. [CrossRef]
14. Rathna, T.; PonnarEttiappan, J.B.; RubenSudhakar, D. Fabrication of Visible-Light Assisted TiO₂-WO₃-PANI Membrane for Effective Reduction of Chromium (VI) in Photocatalytic Membrane Reactor. *Environ. Technol. Innov.* **2021**, *24*, 102023. [CrossRef]
15. Haji Ali, B.; Baghdadi, M.; Torabian, A. Application of Nickel Foam as an Effective Electrode for the Electrochemical Treatment of Liquid Hazardous Wastes of COD Analysis Containing Mercury, Silver, and Chromium (VI). *Environ. Technol. Innov.* **2021**, *23*, 101617. [CrossRef]
16. Thamaraiselvan, C.; Thakur, A.K.; Gupta, A.; Arnusch, C.J. Electrochemical Removal of Organic and Inorganic Pollutants Using Robust Laser-Induced Graphene Membranes. *ACS Appl. Mater. Interfaces* **2021**, *13*, 1452–1462. [CrossRef]

17. Peng, H.; Guo, J. Removal of Chromium from Wastewater by Membrane Filtration, Chemical Precipitation, Ion Exchange, Adsorption Electrocoagulation, Electrochemical Reduction, Electrodialysis, Electrodeionization, Photocatalysis and Nanotechnology: A Review. *Environ. Chem. Lett.* **2020**, *18*, 2055–2068. [[CrossRef](#)]
18. Ferreira-Neto, E.P.; Ullah, S.; Perissinotto, A.P.; de Vicente, F.S.; Ribeiro, S.J.L.; Worsley, M.A.; Rodrigues-Filho, U.P. Prussian Blue as a Co-Catalyst for Enhanced Cr(vi) Photocatalytic Reduction Promoted by Titania-Based Nanoparticles and Aerogels. *New J. Chem.* **2021**, *45*, 10217–10231. [[CrossRef](#)]
19. Yu, M.; Shang, J.; Kuang, Y. Efficient Photocatalytic Reduction of Chromium (VI) Using Photoreduced Graphene Oxide as Photocatalyst under Visible Light Irradiation. *J. Mater. Sci Technol.* **2021**, *91*, 17–27. [[CrossRef](#)]
20. Wang, J.L.; Xu, L.J. Advanced Oxidation Processes for Wastewater Treatment: Formation of Hydroxyl Radical and Application. *Crit. Rev. Environ. Sci. Technol.* **2012**, *42*, 251–325. [[CrossRef](#)]
21. Serge-correales, Y.E.; Ullah, S.; Ferreira-Neto, E.P.; Rojas-mantilla, H.D.; Hazra, C.; Ribeiro, S.J.L. A UV-Visible-NIR Active Smart Photocatalytic System Based on NaYbF₄:Tm³⁺ Upconverting Particles and Ag₃PO₄/H₂O₂ for Photocatalytic Processes under Light on/Light off Conditions. *Mater. Adv.* **2022**, *3*, 2706–2715. [[CrossRef](#)]
22. Amirulsyafiee, A.; Khan, M.M.; Khan, M.Y.; Khan, A.; Harunsani, M.H. Visible Light Active La-Doped Ag₃PO₄ for Photocatalytic Degradation of Dyes and Reduction of Cr(VI). *Solid State Sci.* **2022**, *131*, 106950. [[CrossRef](#)]
23. Ullah, S.; Fayeza; Khan, A.A.; Jan, A.; Aain, S.Q.; Neto, E.P.F.; Serge-Correales, Y.E.; Parveen, R.; Wender, H.; Rodrigues-Filho, U.P.; et al. Enhanced Photoactivity of BiVO₄/Ag/Ag₂O Z-Scheme Photocatalyst for Efficient Environmental Remediation under Natural Sunlight and Low-Cost LED Illumination. *Colloids Surf. A Physicochem. Eng. Asp.* **2020**, *600*, 124946. [[CrossRef](#)]
24. Gomes, L.E.; Nogueira, A.C.; da Silva, M.F.; Plaça, L.F.; Maia, L.J.Q.; Gonçalves, R.V.; Ullah, S.; Khan, S.; Wender, H. Enhanced Photocatalytic Activity of BiVO₄/Pt/PtOx Photocatalyst: The Role of Pt Oxidation State. *Appl. Surf. Sci.* **2021**, *567*, 150773. [[CrossRef](#)]
25. Ullah, S.; Ferreira-Neto, E.P.P.; Hazra, C.; Parveen, R.; Rojas-Mantilla, H.D.D.; Calegaro, M.L.L.; Serge-Correales, Y.E.E.; Rodrigues-Filho, U.P.P.; Ribeiro, S.J.L.J.L. Broad Spectrum Photocatalytic System Based on BiVO₄ and NaYbF₄:Tm₃₊ Upconversion Particles for Environmental Remediation under UV-Vis-NIR Illumination. *Appl. Catal. B* **2019**, *243*, 121–135. [[CrossRef](#)]
26. Shahzad, K.; Tahir, M.B.; Sagir, M.; Kabli, M.R. Role of CuCo₂S₄ in Z-Scheme MoSe₂/BiVO₄ Composite for Efficient Photocatalytic Reduction of Heavy Metals. *Ceram. Int.* **2019**, *45*, 23225–23232. [[CrossRef](#)]
27. Yin, G.; Liu, C.; Shi, T.; Ji, D.; Yao, Y.; Chen, Z. Porous BiVO₄ Coupled with CuFeO₂ and NiFe Layered Double Hydroxide as Highly-Efficient Photoanode toward Boosted Photoelectrochemical Water Oxidation. *J. Photochem. Photobiol. A Chem.* **2022**, *426*, 113742. [[CrossRef](#)]
28. Li, S.; Xing, Z.; Feng, J.; Yan, L.; Wei, D.; Wang, H.; Wu, D.; Ma, H.; Fan, D.; Wei, Q. A Sensitive Biosensor of CdS Sensitized BiVO₄/GaON Composite for the Photoelectrochemical Immunoassay of Procalcitonin. *Sens. Actuators B Chem.* **2021**, *329*, 129244. [[CrossRef](#)]
29. Wei, Y.Y.; Wu, S.H.; Wang, Q.M.; Sun, J.J. A Novel Split-Type Photoelectrochemical Biosensor Based on Double-Strand Specific Nuclease-Assisted Cycle Amplification Coupled with Plasmonic Ag Enhanced BiVO₄ Performance for Sensitive Detection of MicroRNA-155. *Sens. Actuators B Chem.* **2022**, *369*, 132251. [[CrossRef](#)]
30. Ho-Kimura, S.; Soontornchaiyakul, W.; Yamaguchi, Y.; Kudo, A. Preparation of Nanoparticle Porous-Structured BiVO₄ Photoanodes by a New Two-Step Electrochemical Deposition Method for Water Splitting. *Catalysts* **2021**, *11*, 136. [[CrossRef](#)]
31. Chen, M.; Zhao, J.; Huang, X.; Wang, Y.; Xu, Y. Improved Performance of BiVO₄ via Surface-Deposited Magnetic CuFe₂O₄ for Phenol Oxidation and O₂ Reduction and Evolution under Visible Light. *ACS Appl. Mater. Interfaces* **2019**, *11*, 45776–45784. [[CrossRef](#)]
32. Alhaddad, M.; Amin, M.S.; Zaki, Z.I. Novel BiVO₄/ZnO Heterojunction for Amended Photoreduction of Mercury (II) Ions. *Opt. Mater.* **2022**, *127*, 112251. [[CrossRef](#)]
33. Qin, N.; Zhang, S.; He, J.; Long, F.; Wang, L. In Situ Synthesis of BiVO₄/BiOBr Microsphere Heterojunction with Enhanced Photocatalytic Performance. *J. Alloys Compd.* **2022**, *927*, 166661. [[CrossRef](#)]
34. Yang, Z.; Li, H.; Cui, X.; Zhu, J.; Li, Y.; Zhang, P.; Li, J. Direct Z-Scheme Nanoporous BiVO₄/CdS Quantum Dots Heterojunction Composites as Photoanodes for Photocathodic Protection of 316 Stainless Steel under Visible Light. *Appl. Surf. Sci.* **2022**, *603*, 154394. [[CrossRef](#)]
35. Wang, S.; Zhao, L.; Gao, L.; Yang, D.; Wen, S.; Huang, W.; Sun, Z.; Guo, J.; Jiang, X.; Lu, C. Fabrication of Ternary Dual Z-Scheme AgI/ZnIn₂S₄/BiVO₄ Heterojunction Photocatalyst with Enhanced Photocatalytic Degradation of Tetracycline under Visible Light. *Arab. J. Chem.* **2022**, *15*, 104159. [[CrossRef](#)]
36. Pai, H.; Kuo, T.R.; Chung, R.J.; Kubendhiran, S.; Yougbaré, S.; Lin, L.Y. Enhanced Photocurrent Density for Photoelectrochemical Catalyzing Water Oxidation Using Novel W-Doped BiVO₄ and Metal Organic Framework Composites. *J. Colloid Interface Sci.* **2022**, *624*, 515–526. [[CrossRef](#)] [[PubMed](#)]
37. Mahes Kumar, V.; Jiang, Z.; Lin, Y.; Vidhya, B. The Structural and Optical Properties of Ag/Cu Co-Doped BiVO₄ Material: A Density Functional Study. *Mater. Lett.* **2022**, *315*, 131289. [[CrossRef](#)]
38. Prabhavathy, S.; Arivuoli, D. Visible Light-Induced Silver and Lanthanum Co-Doped BiVO₄ Nanoparticles for Photocatalytic Dye Degradation of Organic Pollutants. *Inorg. Chem. Commun.* **2022**, *141*, 109483. [[CrossRef](#)]
39. Sun, W.; Dong, Y.; Zhai, X.; Zhang, M.; Li, K.; Wang, Q.; Ding, Y. Crystal Facet Engineering of BiVO₄/CQDs/TPP with Improved Charge Transfer Efficiency for Photocatalytic Water Oxidation. *Chem. Eng. J.* **2022**, *430*, 132872. [[CrossRef](#)]

40. Srinivasan, N.; Anbuchezhiyan, M.; Harish, S.; Ponnusamy, S. Efficient Catalytic Activity of BiVO₄ Nanostructures by Crystal Facet Regulation for Environmental Remediation. *Chemosphere* **2022**, *289*, 133097. [[CrossRef](#)]
41. Kadam, A.N.; Babu, B.; Lee, S.-W.; Kim, J.; Yoo, K. Morphological Guided Sphere to Dendrite BiVO₄ for Highly Efficient Organic Pollutant Removal and Photoelectrochemical Performance under Solar Light. *Chemosphere* **2022**, *305*, 135461. [[CrossRef](#)]
42. Maheskumar, V.; Lin, Y.M.; Jiang, Z.; Vidhya, B.; Ghosal, A. New Insights into the Structural, Optical, Electronic and Photocatalytic Properties of Sulfur Doped Bulk BiVO₄ and Surface BiVO₄ on {0 1 0} and {1 1 0} via a Collective Theoretical and Experimental Investigation. *J. Photochem. Photobiol. A Chem.* **2022**, *426*, 113757. [[CrossRef](#)]
43. Fatima, H.; Azhar, M.R.; Khiadani, M.; Zhong, Y.; Wang, W.; Su, C.; Shao, Z. Prussian Blue-Conjugated ZnO Nanoparticles for near-Infrared Light-Responsive Photocatalysis. *Mater. Today Energy* **2022**, *23*, 100895. [[CrossRef](#)]
44. Tada, H.; Tsuji, S.; Ito, S. Photodeposition of Prussian Blue Films on TiO₂: Additive Effect of Methanol and Influence of the TiO₂ Crystal Form. *J. Colloid Interface Sci.* **2001**, *239*, 196–199. [[CrossRef](#)] [[PubMed](#)]
45. Lu, J.; Chen, C.; Qian, M.; Xiao, P.; Ge, P.; Shen, C.; Wu, X.L.; Chen, J. Hollow-Structured Amorphous Prussian Blue Decorated on Graphitic Carbon Nitride for Photo-Assisted Activation of Peroxymonosulfate. *J. Colloid Interface Sci.* **2021**, *603*, 856–863. [[CrossRef](#)]
46. Kim, H.; Kim, M.; Kim, W.; Lee, W.; Kim, S. Photocatalytic Enhancement of Cesium Removal by Prussian Blue-Deposited TiO₂. *J. Hazard. Mater.* **2018**, *357*, 449–456. [[CrossRef](#)]
47. Song, Y.Y.; Zhang, K.; Xia, X.H. Photosynthesis and Characterization of Prussian Blue Nanocubes on Surfaces of TiO₂ Colloids. *Appl. Phys. Lett.* **2006**, *88*, 053112. [[CrossRef](#)]
48. Maurin-Pasturel, G.; Long, J.; Guari, Y.; Godiard, F.; Willinger, M.G.; Guerin, C.; Larionova, J. Nanosized Heterostructures of Au@Prussian Blue Analogues: Towards Multifunctionality at the Nanoscale. *Angew. Chem. Int. Ed.* **2014**, *53*, 3872–3876. [[CrossRef](#)]
49. Uchida, H.; Sasaki, T.; Ogura, K. Dark Catalytic Reduction of CO₂ over Prussian Blue-Deposited TiO₂ and the Photo-Reactivation of the Catalyst. *J. Mol. Catal.* **1994**, *93*, 269–277. [[CrossRef](#)]
50. Ghobadi, T.G.U.; Ghobadi, A.; Soydan, M.C.; Vishlaghi, M.B.; Kaya, S.; Karadas, F.; Ozbay, E. Strong Light–Matter Interactions in Au Plasmonic Nanoantennas Coupled with Prussian Blue Catalyst on BiVO₄ for Photoelectrochemical Water Splitting. *ChemSusChem* **2020**, *13*, 2577–2588. [[CrossRef](#)]
51. Meng, X.; Xu, S.; Zhang, C.; Feng, P.; Li, R.; Guan, H.; Ding, Y. Prussian Blue Type Cocatalysts for Enhancing the Photocatalytic Water Oxidation Performance of BiVO₄. *Chem. A Eur. J.* **2022**, *28*, e202201407. [[CrossRef](#)]
52. Li, J.; Chu, Y.; Zhang, C.; Zhang, X.; Wu, C.; Xiong, X.; Zhou, L.; Wu, C.; Han, D. CoFe Prussian Blue Decorated BiVO₄ as Novel Photoanode for Continuous Photocathodic Protection of 304 Stainless Steel. *J. Alloy. Compd.* **2021**, *887*, 161279. [[CrossRef](#)]
53. Yuan, D.; Sun, M.; Tang, S.; Zhang, Y.; Wang, Z.; Qi, J.; Rao, Y.; Zhang, Q. All-Solid-State BiVO₄/ZnIn₂S₄ Z-Scheme Composite with Efficient Charge Separations for Improved Visible Light Photocatalytic Organics Degradation. *Chin. Chem. Lett.* **2020**, *31*, 547–550. [[CrossRef](#)]
54. Yuan, D.; Sun, M.; Zhao, M.; Tang, S.; Qi, J.; Zhang, X.; Wang, K.; Li, B. Persulfate Promoted ZnIn₂S₄ Visible Light Photocatalytic Dye Decomposition. *Int. J. Electrochem. Sci.* **2020**, *15*, 8761–8770. [[CrossRef](#)]
55. Yu, L.; Achari, G.; Langford, C.H. LED-Based Photocatalytic Treatment of Pesticides and Chlorophenols. *J. Environ. Eng.* **2014**, *139*, 1146–1151. [[CrossRef](#)]
56. Izadifard, M.; Achari, G.; Langford, C. Application of Photocatalysts and LED Light Sources in Drinking Water Treatment. *Catalysts* **2013**, *3*, 726–743. [[CrossRef](#)]
57. Tada, H.; Saito, Y.; Kawahara, H. Photodeposition of Prussian Blue on TiO₂ Particles. *J. Electrochem. Soc.* **1991**, *138*, 140–144. [[CrossRef](#)]
58. Jang, S.C.; Hong, S.B.; Yang, H.M.; Lee, K.W.; Moon, J.K.; Seo, B.K.; Huh, Y.S.; Roh, C. Removal of Radioactive Cesium Using Prussian Blue Magnetic Nanoparticles. *Nanomaterials* **2014**, *4*, 894–901. [[CrossRef](#)]
59. Baggio, B.F.; Vicente, C.; Pelegrini, S.; Cid, C.C.P.; Brandt, I.S.; Tumelero, M.A.; Pasa, A.A. Morphology and Structure of Electrodeposited Prussian Blue and Prussian White Thin Films. *Materials* **2019**, *12*, 1103. [[CrossRef](#)]
60. Yu, J.; Kudo, A. Effects of Structural Variation on the Photocatalytic Performance of Hydrothermally Synthesized BiVO₄. *Adv. Funct. Mater.* **2006**, *16*, 2163–2169. [[CrossRef](#)]
61. Packiaraj, R.; Venkatesh, K.S.; Devendran, P.; Bahadur, S.A.; Nallamuthu, N. Structural, Morphological and Electrochemical Studies of Nanostructured BiVO₄ for Supercapacitor Application. *Mater. Sci. Semicond. Process.* **2020**, *115*, 105122. [[CrossRef](#)]
62. Mousavi-Kamazani, M. Facile Hydrothermal Synthesis of Egg-like BiVO₄ Nanostructures for Photocatalytic Desulfurization of Thiophene under Visible Light Irradiation. *J. Mater. Sci. Mater. Electron.* **2019**, *30*, 17735–17740. [[CrossRef](#)]
63. Kulesza, P.J.; Malik, M.A.; Denca, A.; Strojek, J. In Situ FT-IR/ATR Spectroelectrochemistry of Prussian Blue in the Solid State. *Anal. Chem.* **1996**, *68*, 2442–2446. [[CrossRef](#)]
64. Zhou, B.; Qu, J.; Zhao, X.; Liu, H. Fabrication and Photoelectrocatalytic Properties of Nanocrystalline Monoclinic BiVO₄ Thin-Film Electrode. *J. Environ. Sci.* **2011**, *23*, 151–159. [[CrossRef](#)] [[PubMed](#)]

-
65. Li, X.; Wang, J.; Rykov, A.I.; Sharma, V.K.; Wei, H.; Jin, C.; Liu, X.; Li, M.; Yu, S.; Sun, C.; et al. Prussian Blue/TiO₂ Nanocomposites as a Heterogeneous Photo-Fenton Catalyst for Degradation of Organic Pollutants in Water Xuning. *Catal. Sci. Technol.* **2015**, *5*, 504–514. [[CrossRef](#)]
 66. Cheng, K.L.; Ueno, K.; Imamura, T. *Handbook of Organic Analytical Reagents*, 2nd ed.; CRC Press: Boca Raton, FL, USA, 1992; ISBN 9781315140568.
 67. Ishibashi, K.I.; Fujishima, A.; Watanabe, T.; Hashimoto, K. Detection of Active Oxidative Species in TiO₂ Photocatalysis Using the Fluorescence Technique. *Electrochem. Commun.* **2000**, *2*, 207–210. [[CrossRef](#)]